



Cite this: DOI: 10.1039/c8nr05203d

Wulff in a cage gold nanoparticles as contrast agents for computed tomography and photoacoustic imaging†

Maryam Hajfathalian,^a Ahmad Amirshaghghi,^b Pratap C. Naha,^a Peter Chhour,^b Jessica C. Hsu,^b Keely Douglas,^b Yuxi Dong,^b Chandra M. Sehgal,^b Andrew Tsourkas,^b Svetlana Neretina^c and David P. Cormode^{*a,b}

Nanostructures have potential for use in biomedical applications such as sensing, imaging, therapeutics, and drug delivery. Among nanomaterials, gold nanostructures are of considerable interest for biomedical research, owing to their bio-inertness, controllable surface chemistry, X-ray opacity, and optical properties. Gold nanocages are particularly attractive for imaging and therapeutic applications, because they strongly absorb light in the near infra-red region which has high light transmission in tissue. However, the X-ray attenuation of nanocages is relatively low due to their hollow structure. In this study, for the first time, we sought to combine the attractive optical properties of nanoshells with the high payloads of solid nanoparticles and investigated their biomedical applications. Here, we report the engineering of Wulff in a cage nanoparticles *via* converting gold Wulff-shaped seeds into gold–silver core–shell structures and then performing a galvanic replacement reaction. The structure of these nanoparticles was determined using transition electron microscopy. This morphological transformation of gold nanoparticles shaped as truncated octahedrons into a complex Wulff in a cage nanoparticles during the reaction resulted in extensive changes in their optical properties that made these unique structures a potential contrast agent for photoacoustic imaging. We found that the Wulff in a cage nanoparticles had no adverse effects on the viabilities of J774A.1, Renca, and HepG2 cells at any of the concentrations tested. *In vitro* and *in vivo* experiments showed robust signals in both photoacoustic imaging and computed tomography. To the best of our knowledge, this is the first report of Wulff in a cage nanoparticles serving as a platform for multiple imaging modalities. This unique multifunctional nanostructure, which integrates the competencies of both core and shell structures, allows their use as contrast agents for photoacoustic imaging, computed tomography and as a potential agent for photothermal therapy.

Received 28th June 2018,
Accepted 24th September 2018

DOI: 10.1039/c8nr05203d

rsc.li/nanoscale

Introduction

Gold nanoparticles (AuNP) are of considerable interest for biomedical applications, owing to their combination of low-toxicity, well-defined surface chemistry, ease of functionalization, straightforward synthesis methods, and tunable optical properties.^{1–4} They are excellent contrast agents for several

medical imaging modalities. One of the most commonly used medical imaging techniques is computed tomography (CT), a whole-body imaging method. Considerable attention has been directed toward the development of nanoparticles as CT contrast agents over the past decade.^{5,6} Many advantages have been discovered for nanoparticles as CT contrast agents in comparison to small molecules, such as the potential for cell tracking, long circulation times, and targeted imaging applications.⁷ Solid AuNP have been extensively considered as contrast agents for CT due to their strong X-ray attenuation, and their high payload delivery due to their high density.^{7,8}

Plasmonic nanostructures made of noble metals such as gold are also attractive for imaging applications such as photoacoustic imaging (PA) because they can have strong scattering and absorption in the near infra-red region (NIR), where biological tissues absorb the light the least. PA is based on the thermoelastic expansion of a contrast agent or a tissue that

^aDepartment of Radiology, Perelman School of Medicine of the University of Pennsylvania, Philadelphia, Pennsylvania 19104, USA. E-mail: dcormode@upenn.edu

^bDepartment of Bioengineering, School of Engineering and Applied Sciences, University of Pennsylvania, Philadelphia, Pennsylvania 19104, USA

^cCollege of Engineering, University of Notre Dame, Fitzpatrick Hall, Notre Dame, Indiana 46556, USA

† Electronic supplementary information (ESI) available: The supporting information contains additional characterization data of the WICN platform. See DOI: 10.1039/c8nr05203d

occurs when exposed to pulsed laser excitation. The thermoelastic expansion leads to the generation of ultrasonic waves that can be detected by transducers and converted into images.^{9–12} The advantages of CT in vascular imaging are its high spatial and temporal resolution and ability to provide whole body three-dimensional images. However, it has poor soft-tissue contrast. On the other hand, PA can produce images in real-time in localized regions. Thus, these imaging modalities provide complementary information.¹³ Although spherical AuNP produce strong X-ray contrast and have been studied as potential CT contrast agents, they do not provide strong contrast for PA imaging due to the fact that they do not absorb in the NIR region.¹⁴ Therefore, engineering AuNP characteristics such as shape, size, and composition could help to establish a multimodal structure that is an effective platform for both CT and PA imaging techniques.^{13,15–19} Shape engineering of AuNP to create agents for biomedical applications has attracted many researchers in recent years. For example, silica-gold shells for photothermal therapy (PTT) and magnetic resonance imaging were reported by Cho *et al.*²⁰ and gold nanostars have been developed for fluorescence imaging and PTT.²¹ Gold nanorods have been used for multispectral optoacoustic tomography.²² Among these complex morphologies, gold nanocages, which are characterized by porous walls, hollow interiors and tunable thicknesses, have received particular attention for biomedical applications such as drug delivery, imaging and photothermal ablation.^{23,24} However they have not been studied for their CT contrast enhancement. Here, we developed a novel morphology of AuNP entrapped in gold–silver alloy nanocages to integrate the competencies of both solid cores and shells and thereby provide a promising new diagnostic platform by combining dual CT and PA imaging.

In this study, Wulff in a cage nanoparticles (WICN) were synthesized, and characterized using transition electron

microscopy (TEM), UV-vis spectroscopy, inductively coupled plasma-optical emission spectroscopy (ICP-OES), and energy dispersive X-ray spectroscopy (EDS). The Wulff in a cage structure expressed by these nanoparticles was confirmed using TEM. They are of considerable interest for imaging techniques such as CT and PA due to their high X-ray attenuation, biocompatibility, and plasmonic behaviour. The effect of the WICN on the viability of several cell lines was investigated *via* the LIVE/DEAD assay. CT and PA phantom imaging was carried out at different concentrations of WICN. The potential use of WICN for PTT was also considered *via in vitro* experiments. Finally, *in vivo* imaging with CT and PA was carried and their biodistribution determined using ICP-OES.

Results

The synthesis of WICN began with the formation of 16 nm AuNP seeds (Fig. 1A), using a modified Turkevich method.²⁵ These seeds were used as nucleation sites upon which to grow further gold to form 68 nm diameter AuNP.²⁶ These 68 nm AuNP (Fig. 1B) were then heated to 90 °C and poured into aqueous ascorbic acid (AA) of the same temperature. Aqueous AgNO₃ was then injected into the solution of Au seeds and AA. This causes Ag⁺ ions to be reduced by AA to Ag⁰, which leads to their deposition onto the Au particles, producing Au@Ag core-shell structures (Fig. 1C). The solution was cooled in ice and, after purification through centrifugation, the collected core-shell structures were used for the next step of shape engineering, *i.e.* to create nanocage structures. The Au@Ag core-shell structures and aqueous HAuCl₄ were heated to 90 °C separately, before the HAuCl₄ was added to the core-shell structure solution dropwise, which initiated the galvanic replacement reaction (GRR) on the Ag shell. The Ag shell plays the role of a sacrificial template in the galvanic replacement

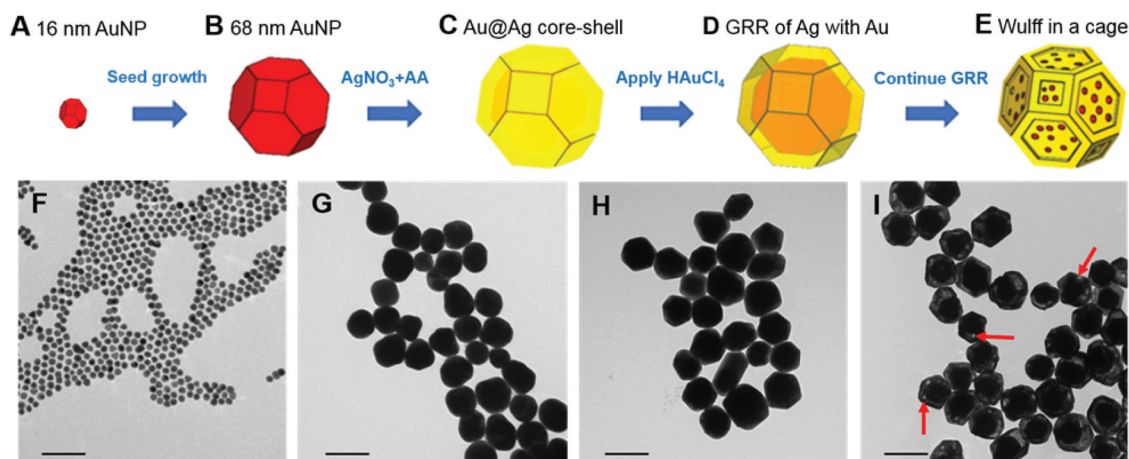


Fig. 1 Synthetic scheme and corresponding TEM of WICN formation. The procedure involves (A) making 16 nm Au seeds, (B) growing the seeds to be 68 nm in diameter, (C) formation of a Ag shell around the Au cores *via* the reduction of Ag⁺ by AA, (D) GRR of Ag with Au to form an AuAg nanoshell, and (E) transforming the nanoshell into a nanocage. TEM images of (F) 16 nm Au seeds, (G) the 68 nm Au seeds used as template, (H) Au@Ag core-shell structures, (I) WICN synthesized using GRR (arrows show the porosities on the cage). The scale bar is 100 nm in each panel.

process, where the oxidation of three Ag^+ ions from the shell occurs for the reduction of each Au^{3+} ion in the solution. So, as Au^{3+} ions are reduced, they form a nanoshell, which alloys with the underlying Ag (Fig. 1D). The addition of aqueous HAuCl_4 leads to a spontaneous oxidation–reduction reaction where HAuCl_4 is reduced and silver is oxidized. The 1:3 replacement ratio of Ag^+ to Au^{3+} causes porosities to form in the shells, leading to the development of an AuAg structure that we termed a cage, which envelops the pre-existing Au cores (Fig. 1E).^{27,28} The WICN were then coated with mPEG (2 kDa) containing thiol groups to provide stability in biological fluids.

Fig. 1F–I shows TEM performed upon samples taken at different stages of the WICN synthesis. Fig. 1F shows 16 ± 1 nm Au seeds that were used to form AuNP whose average diameter was 68 ± 3 nm (Fig. 1G). The Au@Ag core–shell structures (85 ± 4 nm) are shown in Fig. 1H, while a micrograph of WICN, which are 84 ± 2 nm in diameter, is displayed in Fig. 1I. The hydrodynamic sizes, as measured by dynamic light scattering (DLS), of the Au seeds was 15 ± 3 nm, the AuNP was 69 ± 4 nm, Au@Ag core–shell structures 85 ± 2 nm, and WICN 84 ± 1 nm, similar to the measurements from TEM. The galvanic replacement reaction can be controlled and stopped at the stage that provides the desired plasmon peak in the NIR region, as well as stable structures. The reaction, however, must be halted at the level of GRR that yields a porous shell that covers the entire Au core. If the reaction is allowed to continue further, the cage can fragment into pieces, which is undesirable since this product is heterogeneous and cores can become completely separated from shells (Fig. S1†). ICP-OES analysis of WICN revealed their metallic component to be $76 \pm 2\%$ Au and $24 \pm 4\%$ Ag by mass, which was supported *via* EDS measurements (Fig. S2†).

Fig. 2A, shows the optical features of the gold nanostructures at different stages of the synthesis. The extinction spectrum of 68 nm AuNP (pink line) exhibits a sharp plasmon resonance at 537 nm, which is expected for AuNP of this size.^{29,30} A second peak appears at 412 nm for the Au@Ag core–shell structures, which is in agreement with data previously published for similar structures.^{27,31} For the WICN, the absorbance at 412 nm is diminished, and the emergence of a second peak in the NIR at 756 nm is apparent.

The effect of adding varying amounts of the HAuCl_4 solution to the Au@Ag core–shell structures (*i.e.*, increasing the extent of the GRR) on the UV/vis absorption spectra of WICN is shown in Fig. S3.† The intensity of the 746 nm peak increases as the GRR proceeds, which can be explained by the generation of pinholes in these structures.³² Since light in the NIR region (*e.g.*, 650–1000 nm) can penetrate soft tissues relatively well, the optical properties of WICN are well-suited for applications such as contrast agents for PA or PTT agents.^{13,33}

Given the possibility of toxicity arising from silver ion release, we examined the release of silver ions from WICN (Fig. S4†). The silver was released from WICN over 7 days is low (less than 0.1%), which is seven-fold lower than that found for pure silver nanoparticles. This result agrees with prior work that showed that alloying silver with gold suppressed

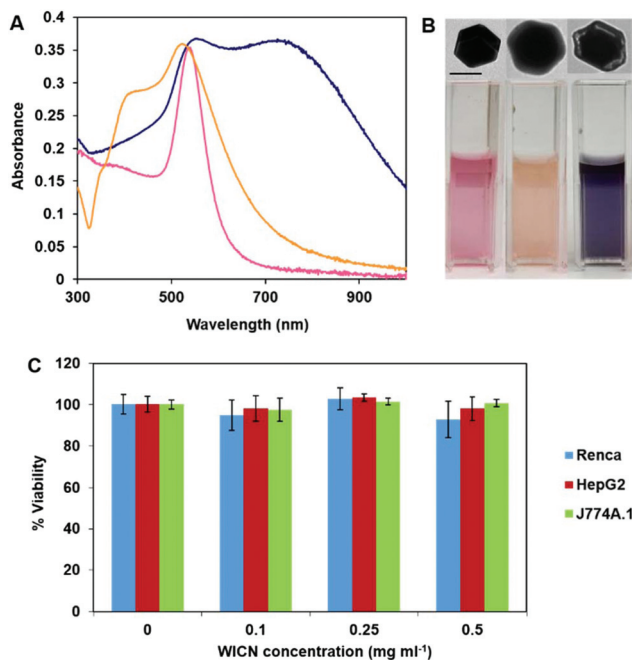


Fig. 2 (A) The optical extinction spectra for the different nanostructures formed: AuNP (pink line), Au@Ag core–shell structures (orange line), and WICN (dark blue line). (B) Photographs of solutions of the different structures showing the color change which occurs during the shape engineering of gold Wulff structures, as well as corresponding TEM images (the scale bar is the same in each panel and it is equal to 50 nm). (C) Effect of WICN on the viability of several cell lines.

silver ion release.³⁴ The effect of WICN on the viability of the J774A.1 (macrophage), HepG2 (hepatocyte), and Renca (renal) cell lines was investigated *via* the LIVE/DEAD assay. We selected these cell lines since they are derived from the liver and kidney, organs that have high exposure to nanoparticles post-injection. The cells were treated with WICN for 24 h at concentrations of 0, 0.1, 0.25, and 0.5 mg WICN (*i.e.*, total metal weight per ml). It was found that WICN did not significantly affect the viability of these cell types (Fig. 2C). These results indicate that the WICN are biocompatible under the conditions tested.

Next, CT and PA phantom imaging were done to demonstrate the feasibility of WICN as a contrast agent for these modalities. Several concentrations of WICN were scanned using a clinical CT scanner at 80, 100, 120, and 140 kV. WICN samples produced strong CT attenuation, which was linearly correlated ($R^2 = 0.99$) with the WICN concentration (Fig. 3A and B). The results showed a slight decrease in CT attenuation from 80 kV to 140 kV, which is in line with previous studies of Au–Ag alloyed NP.³⁴ We found that WICN attenuates X-rays comparably with iopamidol (an FDA-approved iodine-based contrast agent) as presented in Fig. S5.†^{34,35}

Moreover, we compared the CT contrast production of WICN with solid spherical AuNP that are similar in size (79 ± 10 nm, Fig. S6†). As expected, for a given metal concentration, we found the CT attenuation to be the same for both formulations (Fig. S7†).

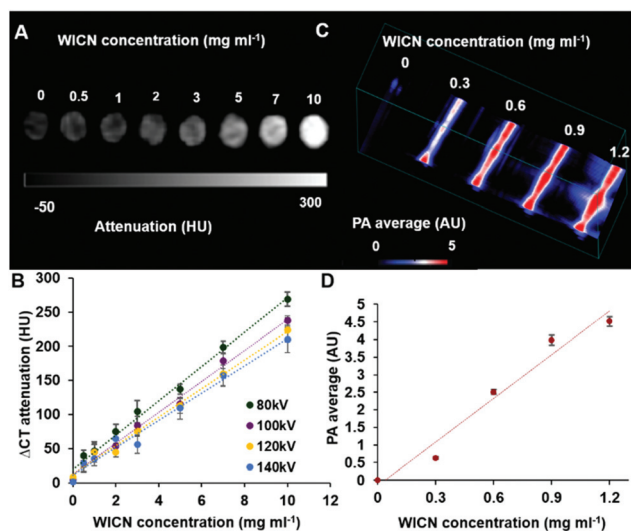


Fig. 3 (A) CT phantom images of various WICN concentrations acquired at 80 kV. (B) CT attenuation of WICN at different X-ray tube voltages. (C) PA phantom images of WICN samples at different concentrations. (D) Quantification of PA intensity versus WICN concentrations.

The PA properties were examined using an experimental system. Different WICN concentrations (0, 0.3, 0.6, 0.9, and 1.2 mg ml⁻¹) were imaged at a laser wavelength of 750 nm (Fig. 3C and D). Significant PA signal was observed, which increased with increasing concentration of WICN, as has been reported for other gold nanostructures.^{35,36}

To assess *in vivo* CT imaging performance, mice were injected with WICN *via* the tail vein at a dose of 250 mg kg⁻¹. Pre-injection and 5 min, 30 min, 1 h, and 2 h post-injection CT scans were done. An increase in CT attenuation in the heart was observed after 5 min which shows the circulation of these novel structures in the blood (Fig. 4A and B).³⁴ The signal in the blood decreased over time and increases in signal in the liver and spleen were observed.^{15,34}

The biodistribution of WICN at 2 h post-injection is shown in Fig. 4C. It is clear that most of the gold and silver was found in the spleen and liver, which is in agreement with previously reported research on similar agents.^{37,38} The amounts of gold that were accumulated in organs were higher than silver; however more silver was observed in urine. This suggests the WICN structure may release some silver, which could be

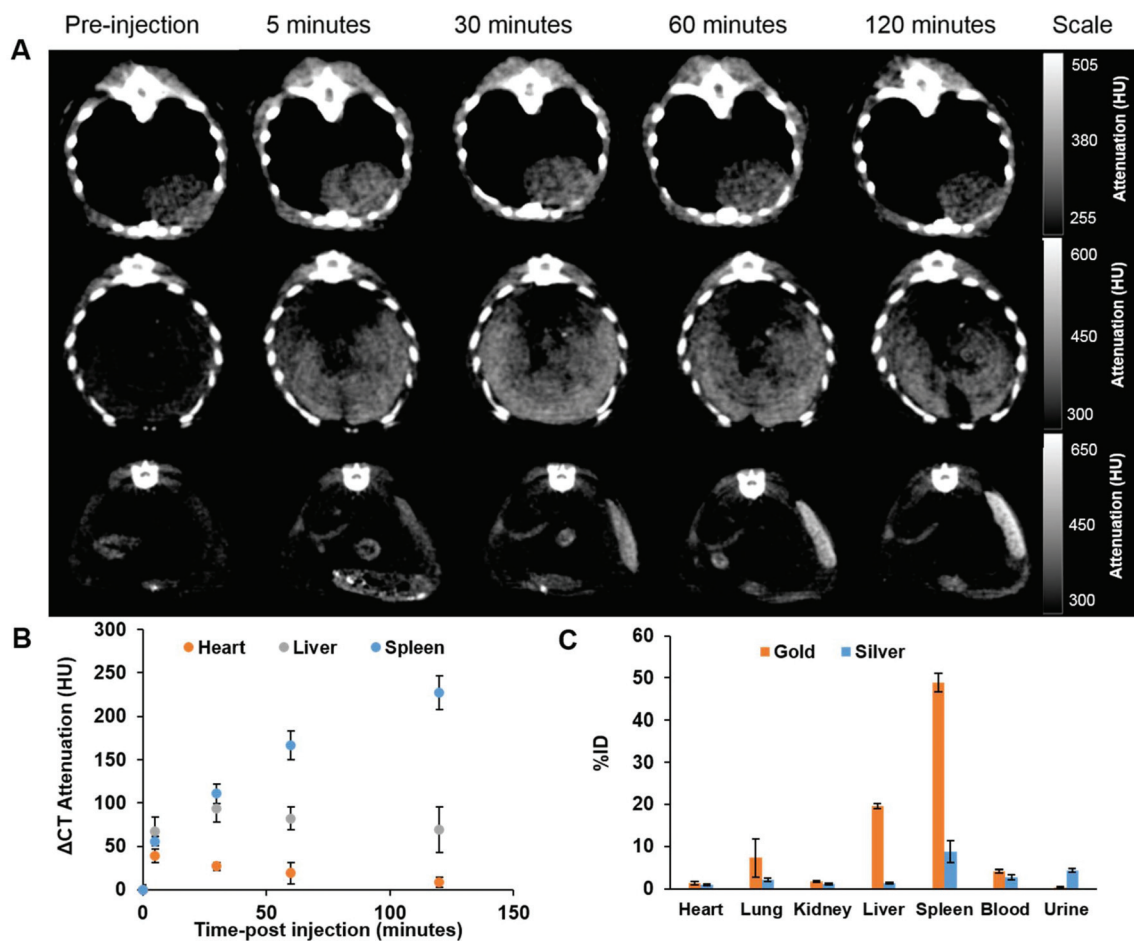


Fig. 4 *In vivo* CT imaging of WICN. (A) Two-dimensional CT images of the heart (top), liver (middle), and spleen (bottom) of a mouse injected with WICN. (B) Quantification of attenuation changes after WICN injection in the heart, liver, and spleen at different time points. (C) The biodistribution of WICN at 2 h post-injection in different organs.



Fig. 5 *In vivo* PA imaging using WICN. (A) A schematic of the PA imaging experiment. Greyscale ultrasound images with PA images overlaid in red (B) before injection of the WICN, and (C) 1 min post-injection of WICN. The arrows show a blood vessel of the mouse before injection.

excreted *via* the urine. No adverse effects of WICN administration were observed in these mice, although more extensive *in vivo* studies are needed to determine the *in vivo* biocompatibility of WICN.

In vivo vascular imaging PA experiments were performed on mice as is shown schematically in Fig. 5A. After injecting the WICN nanoparticles through the mouse tail vein, the NIR pulsed light is absorbed by WICN and PA waves are generated *via* thermoelastic expansion and detected by transducers. Images were reconstructed using a Vevo LAZR system. PA images of the legs of mice showed strong vascular contrast after injection with WICN (15 mg kg^{-1}), while no signal was detected prior to WICN injection (Fig. 5B and C). Moreover, similar results were observed from 2D and 3D PA images of the mouse's tail before and after the injection of WICN (Fig. S8†). The signal-to-background ratio (SBR) of the veins in PA images increased 32-fold after injection of WICN as compared to pre-injection. A link to the real-time movie of the injection of WICN is also presented in the ESI (S9†).

Discussion

In this study, we have synthesized noble metals nanoparticles of unique structure with a high degree of control over chemical, morphological, and optical properties. These WICN structures consist of gold and silver, which are both plasmonic nanomaterials, and have a strong peak in the NIR region, making them an ideal candidate for theranostic applications.^{39–42} Although, spherical AuNP have been found to be effective CT contrast agents due to their high X-ray attenuation and biocompatibility, engineering of their shape to create light absorption in the NIR region can allow them to be used for PA and PTT. Indeed, preliminary *in vitro* PTT studies showed that WICN solutions increased in temperature by as much as $50 \text{ }^\circ\text{C}$ when exposed to NIR laser beam (Fig. S10†).

Other groups have studied empty gold nanocages as contrast agents for different combinations of imaging modalities to CT and PA.^{43–45} For example, Zhang *et al.* reported the two- and three-photon luminescence capabilities of gold nanocages, which allowed cell tracking using two-photon microscopy and photoacoustic microscopy.⁴³ Wang *et al.*

reported an iron oxide-gold nanocage composite that functioned as a bimodal contrast agent for MRI and CT.⁴⁶

However, to our knowledge, this is the first report of the synthesis of solution-based Wulff-in-a-cage nanostructures and their examination as a multifunctional contrast agent that couples the benefits of a solid core and a shell to create strong contrast for both CT and PA. We calculated the payloads of WICN and empty nanocages (see ESI† for details). In WICN structures with a core inside the cage, CT contrast generation on a per nanoparticle basis will be almost 5 times more than empty nanocages due to their higher payloads. This would lead to more balanced contrast generation between CT and PA. Moreover, this could mean that it is not possible to achieve the concentrations needed for CT contrast agent injections with empty nanocages. The utility of this agent is also demonstrated by the complementary information that could be gained from the two imaging methods. While CT provided whole body images at set time points, PA allowed acquisition of images in real time, as evidenced by the movie in the ESI (S9†). We have demonstrated WICN as a biocompatible contrast agent that has no effect on the viability of different cell lines. This platform has a plasmon peak in the NIR region that can be tuned by controlling the degree of GRR during the synthesis. This absorbance makes them an effective contrast agent for PA and a potential agent for PTT. *In vivo* imaging showed that WICN are an effective contrast agent. They accumulated in the liver and spleen as is expected for large nanoparticles.^{47–49} These agents may be able to accumulate in tumors and prove useful for their detection or treatment.^{50,51} The excretion of silver *via* urine was unexpected and may indicate breakdown of the nanoparticles *in vivo*, although preferential clearance of silver has been observed in prior studies of Au–Ag nanoparticles.³⁴

Further development of this work could include exploration of their porous shell for drug encapsulation and delivery. Moreover, interactions generated between the core and shell may make them of interest to other imaging modalities such as surface-enhanced Raman scattering (SERS). These structures could also be targeted with antibodies or peptides to allow target specific imaging with PA or CT. Their NIR absorption could be additionally exploited for photothermal therapy applications, as noted above.

Conclusions

In summary, gold nanostructures have received particular attention in biomedical applications, due to their attractive properties such as bio-inertness and plasmonic resonances. We have formed a new platform in which the reaction of Au–Ag core–shell structures form WICN. This platform is particularly attractive because of its strong absorption peak in the near-infrared, where biological tissues absorb the light the least, and high payload of gold per nanoparticle. These bio-compatible nanoparticles produce strong contrast in both PA and CT imaging techniques and represent an interesting platform for further exploration in other biomedical applications such as PTT.

Experimental methods

Materials

99.9999% silver nitrate (AgNO_3), 99.9999% chloroauric acid (HAuCl_4), 99% sodium citrate dihydrate, and 99% L-ascorbic acid (AA) were obtained from Sigma Aldrich (St Louis, MI). Poly(ethylene-glycol) with a methoxy distal group (mPEG) and a thiol group at the other end of the polymer was purchased from Creative PEGWorks (Winston Salem, NC, USA). Deionized (DI) water with a resistivity of $18.2 \text{ M}\Omega \text{ cm}^{-1}$ was used for the preparation of all aqueous solutions. Before each experiment, all glassware was cleaned with aqua regia (3 parts HCl, 1 part HNO_3 and 1 part water) and rinsed with DI water three times.

WICN synthesis

A modified Turkevich method was used to synthesize spherical AuNP 15 nm in diameter.²⁵ A mixture of 60 ml of DI water and 600 μl of 1% chloroauric acid (HAuCl_4) was heated to boiling point. 1.8 ml of 1% sodium citrate dihydrate was then added to the solution. After heating for 15 min the solution was allowed to cool to room temperature while stirring for 5 h. AuNP 68 nm in diameter were then synthesized using a seeded growth method where the aforementioned 15 nm AuNP were used as seeds.¹⁹ 1 ml of 1% HAuCl_3 was added to 100 ml of DI water at room temperature, followed by the addition of 750 μl of 15 nm AuNP prepared as described above. The growth of AuNP was initiated by adding 220 μl of 1% sodium citrate dihydrate and 1 ml of 0.03 M hydroquinone. The mixture was then stirred for 3 h at room temperature and purified *via* centrifugation at 1400 rcf for 12 min (the supernatant was discarded and the pellet was re-suspended in 50 ml of DI water).

Core–shell nanoparticles were formed by the reduction of silver nitrate onto the 68 nm AuNP. First, 5 ml of the 68 nm Au seed solution (as prepared above) was heated to 90 °C. Upon reaching this temperature, the seeds were immediately poured into 1 ml of 1 mM AA that had also been heated to 90 °C. Then, 3 ml of aqueous AgNO_3 (1 mM), which was also heated to 90 °C, was added in a dropwise manner over a 2 min interval. The reaction was then allowed to continue for 10 min, after which the solution was cooled in an ice bath for 15 min.

The Au@Ag nanoparticles were collected *via* centrifugation at 1400 rcf for 12 min. The supernatant was discarded and the pellet was resuspended in 5 ml of DI water. WICN were formed using a galvanic replacement reaction. 5 ml of Au@Ag core–shell structures, prepared as above, and 10 ml of aqueous HAuCl_4 (300 μM) were preheated to reach 90 °C. WICN were obtained by adding 8 ml of aqueous HAuCl_4 to the Au@Ag core–shell structures in a dropwise manner over a 3 min period.

Then, ligand exchange was performed using 2000 MW poly (ethylene-glycol) with a methoxy distal group (mPEG) to stably cap the gold nanocages. 1 ml of 0.0012 mM thiol-mPEG (2k Da) was added to a solution of WICN as prepared above and the resulting mixture was then allowed to stir overnight. The resulting nanoparticles were collected by centrifugation (at 900 rcf for 10 min) and then sterilized with a 0.45 μm syringe filter (EMD Millipore, Billerica MA).

Solid, spherical AuNP that were used in phantom imaging as a control were synthesized using the same approach as the 68 nm cores above, followed by PEGylation and purification at that point.

Particle characterization

UV-vis spectra were recorded using a UV-vis spectrometer (Thermo-Fisher Scientific, USA). The nanoparticle spectra were recorded from wavelengths of 300 to 1100 nm. TEM of WICN was performed using a JEOL 1010 microscope operating at 80 kV. 5 μl of diluted WICN (2.5 μl WICN was mixed with 2.5 μl DI water) were dropped onto carbon-coated copper grids (FCF-200-Cu, Electron Microscopy Sciences, Hatfield, PA, USA) to prepare all TEM samples. Microscopy was done after allowing the grids to dry at room temperature for 3 h. WICN concentrations were measured using inductively coupled plasma – optical emission spectroscopy (ICP-OES). To determine gold concentrations, three different volumes of sample (5, 10, 15 μl) were dissolved in 1 ml aqua regia (3 parts HCl, 1 part HNO_3 and 1 part water). For silver concentration determination, samples were dissolved in 1 ml nitric acid. The volumes were increased to 10 ml by adding DI water 30 min after acid addition to the samples. The measurements were performed using a Spectro-Genesis ICP (Spectro Analytical Instruments GmbH, Kleve, Germany). A JEOL JEM-1400 transmission electron microscope (JEOL, MA, USA, Inc.) was used to acquire energy dispersive X-ray spectra of WICN at 120 kV. The hydrodynamic diameters of WICN were measured using DLS (Nano ZS-90 Zetasizer, Malvern Instruments, Worcestershire, UK). 100 μl of the WICN structures were diluted to 1 ml with DI water for DLS measurements.

Silver ion release

The release of silver ions from WICN was examined in DI water (note: the media that silver ion release can be assessed in is limited, since chloride ions confound this experiment.³⁴ 100 μl of 50 mg WICN per ml stock was diluted in 4900 μl DI water in 20 ml glass vials. 3 solutions were incubated at 37 °C and samples were collected at 1, 5, 24, 48, 72, 96, 120, 144, and

168 hours. After the desired incubation time, the tubes were centrifuged at 2500 rcf for 10 min. The supernatant was collected and the concentration of silver in the supernatant measured using ICP-OES.

***In vitro* experiments**

The biocompatibility of WICN was studied using J774A.1, HepG2, Renca (ATCC, Manassas, VA). The LIVE–DEAD assay (Life Technologies, Frederick, MD) was used to study their viability under different conditions. The HepG2 and J774A.1 cell lines were cultured in 35 mm dishes with 20 mm glass bottoms by adding 7.5×10^4 cells per dish. Cells were cultured for 24 h at 37 °C, 5% CO₂ with DMEM (10% fetal bovine serum (FBS), 1% streptomycin–penicillin) before additional steps were taken. Renca cells were cultured under the same conditions except that, as per the supplier's instructions, RPMI (10% FBS, 1% streptomycin–penicillin, 0.1 mM NEAA, 1 mM sodium pyruvate, and 2 mM L-glutamine) media was used. After 24 h, the media was removed, and fresh media containing WICN at 0, 0.1, 0.25 or 0.5 mg ml⁻¹ (total metal) was added. The cells were incubated with WICN for 24 h. The cells were then washed with DBPS twice before 400 µl of LIVE/DEAD cocktail was added to the cells (this cocktail consisted of 2 ml of DPBS, 2 µl of stock (used as received) ethidium-1 homodimer, 0.5 µl of stock Calcein AM, and 0.5 µl of 3.2 mM Hoechst 33342). The cells were incubated for 20 min with these reagents. Afterward, a Nikon Eclipse Ti–U fluorescence microscope was used to image the cells. In each case, five images per well were acquired using three filter pairs: 350/461 nm for Hoechst 33342, 495/515 nm for Calcein, and 528/617 nm for Ethidium Homodimer-1 (EthD-1). The images were then analyzed to count the number of live or dead cells in each field. Viability experiments on the same samples were repeated three times.

Computed tomography phantom imaging

Different concentrations of the WICN were prepared in 250 µl vials with three replicates. For this case, WICN were prepared in different concentrations (from 0.5 mg ml⁻¹ to 10 mg ml⁻¹ total metal) and pipetted into PCR tubes. Tubes were then sealed and secured in a plastic rack with Parafilm and then placed in a custom made plastic container which was then filled with water to a height of 21 cm. CT images of this phantom were acquired using a Siemens SOMATOM Force clinical CT scanner at 80, 100, 120, and 140 kV. The tube current used was 360 mA. Images were reconstructed with a slice thickness of 0.5 mm, a matrix size of 512 × 512, and a field of view of 37 × 37 cm. The images were analyzed using OsiriX MD (v.8.0.2 64-bit software) to determine the attenuation values in Hounsfield units (HU) for each concentration. Phantom imaging of similarly sized solid AuNP used the same method and concentrations.

Photoacoustic phantom imaging

Photoacoustic images were acquired using a Vevo Lazr device (VisualSonics, Toronto CA). 40 µl of WICN were placed into

0.5 mm diameter polyethylene tubing, which was covered in 2–3 cm of water. WICN at 0.3, 0.6, 0.9, and 1.2 mg ml⁻¹ (on a total metal basis) were imaged. The PA images were acquired using the following parameters: ultrasound gain +27 dB, PA gain 22 dB, distance 1.1–1.5 cm from the transducer. The LZ550 transducer was used with axial resolution of 44 µm and a broadband frequency of 32–55 MHz.

Photothermal heating

WICN (10 µg ml⁻¹) were exposed to 808 nm diode laser (OEM Laser Systems) at a power of 2 W cm⁻² for 10 min in a quartz cuvette during which changes in the temperature were monitored using an optical thermometer (Qualitrol corporation, NY USA). After reaching a constant temperature, the laser was turned off and the sample was allowed to cool to room temperature. To examine the repeatability of the heat conversion of the WICN, the experiment was repeated three times. The same method was applied to DI water as a control.

***In vivo* computed tomography imaging**

All *in vivo* experimental protocols were conducted in accordance with PHS policy on humane care and use of laboratory animals (Public Law 99–158) and with approval from the Institutional Animal Care and Use Committee of the University of Pennsylvania. The images were acquired using a MicroCAT II (Siemens Healthcare GmbH, Erlangen, Germany) at 80 kV and 500 µA with a 512 × 512 matrix and 100 µm isotropic voxels. C57BL/6J mice ($n = 3$) were anesthetized with isoflurane and pre-scanned before injection of WICN *via* the tail vein at a dose of 250 mg of total metal (gold and silver) per kg. The CT images were analyzed using OsiriX MD (v.8.0.2 64-bit software) to determine the attenuation values in Hounsfield units (HU) for different organs.

***In vivo* photoacoustic imaging**

PA experiments were carried out on nude mice ($n = 3$) which were anesthetized with isoflurane before injection. 15 mg kg⁻¹ WICN was injected *via* the vein tail. The images were acquired using 755 nm excitation light, with ultrasound gain of +27 dB, PA gain 35 dB, and priority 95%. Signal-to-background ratio (SBR) values were calculated from these images. Intensities were measured by placing ROIs on the blood vessels and measuring the signal before and after injection. Values were averaged from six images per animal. The signal in the muscle was then also determined (this was used as the background) and the SBR calculated from these values. The imaging parameters, PA gain, ultrasound gain, and time-gain constant were maintained at the same level for all mice.

Biodistribution

The biodistribution of WICN was determined using ICP-OES. Mice were sacrificed at 2 h after injection of WICN at 250 mg kg⁻¹ ($n = 3$ per dose) and blood samples were then collected. After perfusion with PBS, the liver, lungs, heart, spleen, kidneys, and urine were collected. All the organs were weighed and then chopped into small pieces. The same organs were

used for gold and silver measurements. For these measurements, small pieces of the organs were dissolved in 800 μl of concentrated nitric acid and kept at 75 $^{\circ}\text{C}$ for 20 h, and then 400 μl of the solution was taken for silver content measurement. The volume of this sample was increased to 10 ml by adding DI water. For gold measurements, 200 μl of concentrated hydrochloric acid was also added to 400 μl of the remained digested organ solution and kept for 4 h. Then the volume was increased to 10 ml by adding DI water. The concentrations of gold and silver in these samples were determined using the above mentioned equipment.

Conflicts of interest

There are no conflicts to declare.

Acknowledgements

This work was supported in part with funding provided by the NIH (R01 HL131557, and S10 OD016310). AT acknowledges the funding provided by the NIH (R01-CA181429). JCH acknowledges the support of a National Science Foundation Graduate Research Fellowship (DGE-1321851). We acknowledge Eric Blankemeyer and Susan Schultz from Radiology Department of University of Pennsylvania for their help with the microCT scans and PA scanner, respectively.

References

- R. M. Cabral and P. V. Baptista, *Expert Rev. Mol. Diagn.*, 2014, **14**, 1041.
- J. T. Au, G. Craig, V. Longo, P. Zanzonico, M. Mason, Y. Fong and P. Allen, *Am. J. Roentgenol.*, 2013, **200**, 1347.
- P. V. Baptista, *Expert Rev. Mol. Diagn.*, 2012, **12**, 541.
- M. Shah, V. D. Badwaik and R. J. Dakshinamurthy, *Nanosci. Nanotechnol.*, 2014, **14**, 344.
- N. Lee, S. H. Choi and T. Hyeon, *Adv. Mater.*, 2013, **25**, 2641.
- D. P. Cormode, P. C. Naha and Z. A. Fayad, *Contrast Media Mol. Imaging*, 2014, **9**, 37.
- J. Kim, P. Chhour, J. Hsu, H. I. Litt, V. A. Ferrari, R. Popovtzer and D. P. Cormode, *Bioconjugate Chem.*, 2017, **28**, 1581.
- D. P. Cormode, E. Roessler, A. Thran, T. Skajaa, R. E. Gordon, J. P. Schlomka, V. Fuster, E. A. Fisher, W. J. M. Mulder, R. Proksa and Z. A. Fayad, *Radiology*, 2010, **256**, 774.
- Y. S. Chen, W. Frey, S. Kim, K. Homan, P. Kruizinga, K. Sokolov and S. Emelianov, *Opt. Express*, 2010, **18**, 8867.
- S. J. Yoon, S. Mallidi, J. M. Tam, J. O. Tam, A. Murthy, K. P. Johnston, K. V. Sokolov and S. Emelianov, *Opt. Lett.*, 2010, **35**, 3751.
- A. Hariri, J. Lemaster, J. Wang, A. S. Jeevarathinam, D. L. Chao and J. V. Jokerst, *Photoacoustics*, 2018, **9**, 10.
- N. Dana, T. Sowers, A. Karpiouk, D. Vanderlaan and S. Emelianov, *J. Biomed. Opt.*, 2017, **22**, 106012.
- L. Jing, X. Liang, Z. Deng, S. Feng, X. Li, M. Huang, C. Li and Z. Dai, *Biomaterials*, 2014, **35**, 5814.
- G. Kawamura, M. Nogami and A. Matsuda, *J. Nanomater.*, 2013, **2013**, 1.
- A. J. Mieszawska, W. J. Mulder, Z. A. Fayad and D. P. Cormode, *Mol. Pharm.*, 2013, **10**, 831.
- J. C. Stendahl and A. J. Sinusas, *J. Nucl. Med.*, 2015, **56**, 1469.
- S. E. Skrabalak, J. Chen, L. Au, X. Lu, X. Li and Y. Xia, *Adv. Mater.*, 2007, **19**, 3177.
- Y. Yang, T. Feng, X. Wang, H. Wu, Y. Li, L. Yang, X. Tang and H. Mao, *Med. Phys.*, 2016, **43**, 589.
- P. Chhour, J. Kim, B. Benardo, A. Tovar, S. Mian, H. I. Litt, V. A. Ferrari and D. P. Cormode, *Bioconjugate Chem.*, 2017, **28**, 260.
- P. Diagaradjane, A. Shetty, J. C. Wang, A. M. Elliott, J. Schwartz, S. Shentu, H. C. Park, A. Deorukhkar, R. J. Stafford and S. H. Cho, *Nano Lett.*, 2008, **8**, 1492.
- H. Chen, X. Zhang, S. Dai, Y. Ma, S. Cui, S. Achilefu and Y. Gu, *Theranostics*, 2013, **3**, 633.
- A. Taruttis, N. Lozano, A. Nunes, D. A. Jasim, N. Beziere, E. Herzog, K. Kostarelos and V. Ntziachristos, *Nanoscale*, 2014, **6**, 13451.
- W. Li, X. Cai, C. Kim, G. Sun, Y. Zang, R. Deng, M. Yang, J. Chen, S. Achilefu, L. V. Wang and Y. Xia, *Nanoscale*, 2011, **3**, 1724.
- S. E. Skrabalak, J. Chen, Y. Sun, X. Lu, L. Au, C. M. Copley and Y. Xia, *Acc. Chem. Res.*, 2008, **41**, 1587.
- J. Turkevich and J. Stevenson, *Discuss. Faraday Soc.*, 1951, **11**, 55.
- S. D. Perrault and W. C. Chan, *J. Am. Chem. Soc.*, 2009, **131**, 17042.
- M. Hajfathalian, K. D. Gilroy, A. Yaghoubzade, E. Menumerov, R. A. Hughes and S. Neretina, *ACS Nano*, 2016, **10**, 6354.
- M. Hajfathalian, K. D. Gilroy, R. A. Hughes and S. Neretina, *Small*, 2016, **12**, 3444.
- Y. Xia, W. Li, C. M. Copley, J. Chen, X. Xia, Q. Zhang, M. Yang, E. C. Cho and P. K. Brown, *Acc. Chem. Res.*, 2011, **44**, 914.
- X. Lu, M. Rycenga, S. E. Skrabalak, B. Wiley and Y. Xia, *Annu. Rev. Phys. Chem.*, 2009, **60**, 167.
- Y. Yang, J. Shi, G. Kawamura and M. Nogami, *Scr. Mater.*, 2008, **58**, 862.
- Y. Sun and Y. Xia, *Nano Lett.*, 2003, **3**, 1569.
- W. Li, P. K. Brown, L. V. Wang and Y. Xia, *Contrast Media Mol. Imaging*, 2011, **6**, 370.
- P. C. Naha, K. C. Lau, J. C. Hsu, M. Hajfathalian, S. Mian, P. Chhour, L. Uppuluri, E. S. McDonald, A. D. Maidment and D. P. Cormode, *Nanoscale*, 2016, **8**, 13740.
- R. Cheheltani, R. M. Ezzibde, P. Chhour, K. Pulaparthi, J. Kim, M. Jurcova, J. C. Hsu, C. Blundell, H. I. Litt, V. A. Ferrari, H. R. Allocock, C. M. Sehgal and D. P. Cormode, *Biomaterials*, 2016, **102**, 87.

- 36 Y. S. Chen, S. J. Yoon, W. Frey, M. Dockery and S. Emelianov, *Nat. Commun.*, 2017, **8**, 15782.
- 37 O. Betzer, N. Perets, A. Angel, M. Motiei, T. Sadan, G. Yadid, D. Offen and R. Popovtzer, *ACS Nano*, 2017, **11**, 10883.
- 38 W. H. De Jong, W. I. Hagens, P. Krystek, M. C. Burger, A. J. Sips and R. E. Geertsma, *Biomaterials*, 2008, **29**, 1912–1919.
- 39 W. Lu, Q. Huang, G. Ku, X. Wen, M. Zhou, D. Guzatov, P. Brecht, R. Su, A. Oraevsky, L. V. Wang and C. Li, *Biomaterials*, 2010, **31**, 2617.
- 40 T. Dreifuss, O. Betzer, M. Shilo, A. Popovtzer, M. Motiei and R. Popovtzer, *Nanoscale*, 2015, **7**, 15175.
- 41 A.-Q. Zhang, D.-J. Qian and M. Chen, *Eur. Phys. J. D*, 2013, **67**, 231.
- 42 T. Dreifuss, E. Barnoy, M. Motiei and R. Popovtzer, *Biomedical Imaging*, Springer, Cham., 2017, pp. 403; R. M. Cabral and P. V. Baptista, *Expert Rev. Mol. Diagn.*, 2014, **14**, 1041–1052.
- 43 Y. S. Zhang, Y. Wang, L. Wang, Y. Wang, X. Cai, C. Zhang, L. V. Wang and Y. Xia, *Theranostics*, 2013, **3**, 532–543.
- 44 X. Xia, M. Yang, L. K. Oetjen, Y. Zhang, Q. Li, J. Chen and Y. Xia, *Nanoscale*, 2011, **3**, 950.
- 45 B. Pang, X. Yang and Y. Xia, *Nanomedicine*, 2016, **11**, 1715–1728.
- 46 G. Wang, W. Gao, X. Zhang and X. Mei, *Sci. Rep.*, 2016, **6**, 28258.
- 47 S. Huo, H. Ma, K. Huang, J. Liu, T. Wei, S. Jin, J. Zhang, S. He and X. J. Liang, *Cancer Res.*, 2012, **73**, 1.
- 48 G. Sonavane, K. Tomoda and K. Makino, *Colloids Surf., B*, 2008, **66**, 274.
- 49 S. Hirn, M. Semmler-Behnke, C. Schleh, A. Wenk, J. Lipka, M. Schäffler, S. Takenaka, W. Möller, G. Schmid, U. Simon and W. G. Kreyling, *Eur. J. Pharm. Biopharm.*, 2011, **77**, 407.
- 50 H. Cabral, Y. Matsumoto, K. Mizuno, Q. Chen, M. Murakami, M. Kimura, Y. Terada, M. R. Kano, K. Miyazono, M. Uesaka and N. Nishiyama, *Nat. Nanotechnol.*, 2011, **6**, 815.
- 51 E. A. Sykes, J. Chen, G. Zheng and W. C. Chan, *ACS Nano*, 2014, **8**, 5696.